AUT Journal of Mechanical Engineering

AUT J. Mech. Eng., 7(1) (2023) 73-88
DOI: 10.22060/ajme.2023.21285.6033

Multi-Domain Modeling Platform for Electrical-Signature-Based Condition Monitoring of Motor-Driven Pumps

Zahra Araste, Mohammad Jamimoghaddm, Ali Sadighi *

School of Mechanical Engineering, University of Tehran, Tehran, Iran

ABSTRACT: Due to the vital role of motor-driven pumps in various industries such as oil and gas, manufacturing, chemical, etc., their continuous monitoring and implementing effective maintenance methods is of crucial importance. Periodic inspections and intermittent vibration data collection using accelerometers is among the most common methods. Electrical signature analysis is an alternative approach that only uses electrical measurements for the purpose of fault detection. Despite the unique advantages of this method, such as its non-intrusiveness and possibility of continuous monitoring of the equipment, there have been limited studies on its underlying theory with majority of the proposed ESA-based methods taking data-driven approach towards condition monitoring problem. Data-driven methods rely on the experimental data collected from the equipment to train the statistical models. This imposes a serious limitation on the application of electrical signature analysis and makes the generalization harder. In this paper the electromechanical coupling in a motor-driven centrifugal pump is studied in order to demonstrate the effects of different operating conditions of pump on motor electrical signals. Lumped parameter approach is employed to derive governing equations of the induction motor and computational fluid dynamics is utilized to analyze the interaction of the centrifugal pump blades and fluid. Such a modeling platform presents a physics-based approach towards electrical signature analysis based condition monitoring. A closed-loop hydraulic test rig is built to compare and verify the simulation results.

Review History:

Received: Apr. 01, 2022
Revised: Jan, 14, 2022
Accepted: Mar. 03, 2023
Available Online: Apr. 18, 2023

Keywords:

Centrifugal pump
Electrical signature analysis (ESA)
Computational Fluid Dynamics (CFD)
Lumped parameter m-odel

1- Introduction

Centrifugal pumps are one of the most widely used equipment in the industry with applications in various sectors such as petroleum and petrochemical, agriculture, power generation plants, mining, etc. Therefore, considering the vital role of pumps, continuous monitoring of their operation has an important effect on the performance of plants. Various condition monitoring (CM) methods are employed method for detecting any impending fault which could significantly reduce the cost of repairs by early detection of defects (failures).

The CM methods have been dominated by the techniques that measure vibration, sound, pressure, temperature, and in general, signals which require installation of various sensors on the equipment.[3]-[1] Among these methods, vibration analysis is the most common approach of CM in pumps 4]]. Utilization of high precision accelerometer sensors dramatically increases the overall cost of the system. In addition, the installation of additional sensors requires vast amount of wiring that reduce overall reliability of the system. In addition, in some cases such as submersible pumps, accessing and installing the mechanical sensors may not be feasible. Furthermore, collecting and analyzing the vibration signals are often done periodically that makes early fault detection and continuous monitoring impossible.

In 1989, the idea of using motor electrical signatures for fault detection and diagnosis (FDD) was introduced for the first time in Oak Ridge National Lab [5]. In this approach, more affordable and yet more reliable voltage and current sensors are used instead of the traditional mechanical sensors. In fact, electrical signature analysis enables continuous monitoring of the target equipment at a lower cost [6]– [8].

The cornerstone of the ESA approach is the electromechanical coupling that exists in any electromechanical energy conversion device. Although there are several studies using ESA for FDD, to the best of our knowledge, a comprehensive simulation of this coupling has not been considered in previous works. As an example, in9]], Kallesøe derived this coupling, with some simplifying assumptions, in the form of state space model just for designing an observer that is incorporated in fault detection and isolation scheme. The major goal of this research is to address the dynamics of this coupling theoretically and to further investigate the effects of two common type of faults, including vane tip fault and cavitation, on operational characteristic of the pump and electrical signatures of induction motor and also compare numerical and experimental results.

*Corresponding author's email: asadighi@ut.ac.ir

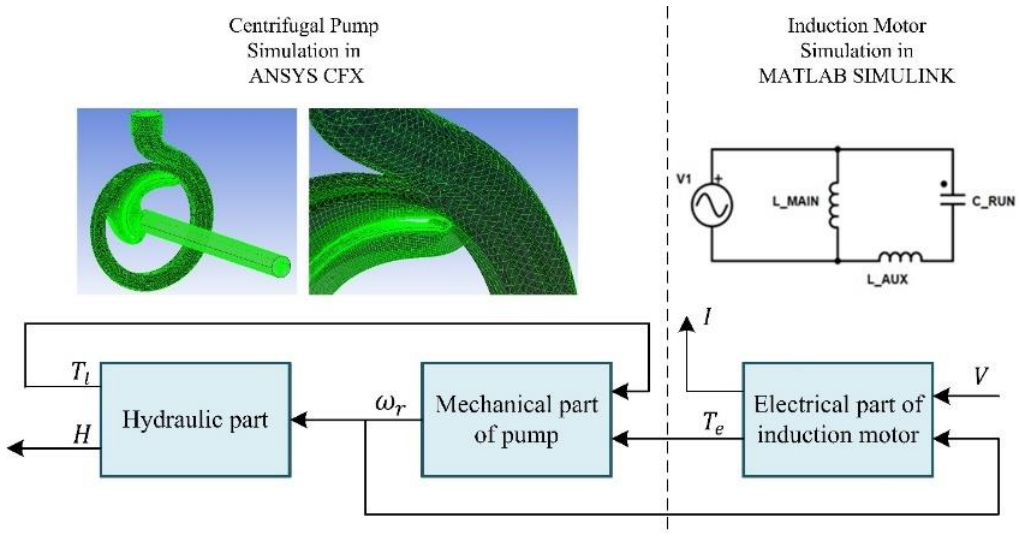

Fig. 1. Schematic of electromechanical energy conversion simulation stages.

One of the challenges we are facing here is the complex fluid-solid interaction (FSI) as occurs in the pump housing which leaves us no choice but to resort to computational fluid dynamics (CFD) techniques11] ,[10]].

CFD provides detailed information about the flow regime and is less expensive than experimental tests. CFD analysis has many applications, one of which is to predict the performance of pumps at off-design operating conditions 12]]. Another application of the CFD is analysis of the effects of various structural parameters on pump performance13]].

In recent years, a lot of research has been done to study centrifugal pump faults using CFD analysis. Zabihi [14] investigated blade tip fault by numerical simulation of pressure fluctuations using Ansys CFX. By comparing the results of experimental tests and numerical simulations, it was shown that the amplitude of power spectrum density at the blade passing frequency (*BPF*) and the shaft rotational frequency is a good criterion for detecting the faulty performance of the pump. Lu et al. [15] carried a numerical simulation of fluid pressure pulsations at the inlet and outlet of a centrifugal pump in order to analyze the cavitation effect on power spectrum density (PSD) of the pressure. Results of this research depicted that under the presence of a severe level of cavitation fault, the dominant frequency at the inlet side of the pump were 0.6 times of the shaft rotation frequency and its amplitude decreases significantly compared to the healthy status. In another research by Lei et al. [16], simulation of a centrifugal pump with influencing cavitation in two off-design conditions was conducted and it is shown that the cavitation has a less severe effect on pressure pulsations on the impeller in flow rates higher than the pump design flow rate.

The electromechanical coupling is analyzed in two steps: In the first step, in which the electrical energy is being converted to mechanical energy, equations of the electric motor are derived using the lumped-parameter approach. In the second step, which occurs in pump impeller and casing, mechanical energy is converted to hydraulic energy. Since employing the lumped-parameter approach for modelling the energy conversion of this step is too complicated, CFD is utilized to simulate this step. The two steps of energy conversion and related inputs and outputs are shown in Fig. 1.

Section 2 presents numerical modeling of the pump and the lumped-parameter model of the induction motor is explained in section 3. A closed hydraulic test rig for experimental investigation is presented in section 4. In section 5, the results of the numerical simulation are confirmed through experiments.

2- CENTRIFUGAL PUMP NUMERICAL MODEL

In this research, a DAB K12/200M single volute, single suction centrifugal pump, with main parameters listed in Table 1 was studied. In order to conduct numerical simulations, the commercial software, ANSYS-CFX 18.1 was employed. The 3-D point cloud technique was used to obtain the 3-D model of casing and impeller of the pump and the fluid inside the volute is obtained using SolidWorks software. In order to establish a suitable mesh, Ansys meshing and ANSYS TURBOGRID software were employed to generate volute and impeller meshes. The resultant meshed parts are shown in Fig. 1. Given the symmetric geometry of the blades, only one-third of the complete impeller geometry was modeled with the aim of reducing computational cost. Turbulence model used in this work was the SST turbulence model which uses $k-\epsilon$ model in the region far from the wall and the $k-\omega$ model in the near-wall region. The transient analysis was conducted by adopting 1-degree rotation of the impeller per step and 10 complete turns of the impeller.

Table 1. Main Parameters of Pump

Parameters	Unit	Value
Number of blades	-	3
Impeller diameter	mm	120
Pump inlet and outlet diameter	inch	1 ½
Rotational speed	rpm	2900
Pump nominal power	Hp5	1
Flowrate at best eefficiency point (BEP)	m^3/h	12
Head at best eefficiency point (BEP)	m	11.5

Table 2. Mesh Independency Study

Number	Element No.	Efficiency (%)	Eefficiency reduction (%)	Head	Head reduction (%)
1	985392	65.203	-	13.74027	-
2	1115392	63.430	2.720	14.16431	3.086
3	2719441	62.075	2.137	14.07175	0.653
4	3349340	62.301	0.364	14.24953	1.263
5	4395012	62.083	0.350	14.18411	0.459

Three different conditions are considered for simulation: (1) Simulation in healthy condition, (2) Simulation with presence of vane tip fault, (3) Simulation of the pump under cavitation conditions for a certain flow rate. Besides, the simulated flow was assumed to be incompressible at the steady state condition.

Another factor that has notable influence on the acceleration of the numerical convergence of the solution is selection of appropriate boundary conditions (B.C.) [17]. Several options are available for applying the inlet and outlet boundary conditions in Ansys CFX, among them three combinations have been used more frequently [18]:

Inlet B.C. of pump: total pressure
Outlet B.C. of pump: mass flow
Inlet B.C. of pump: mass flow
Outlet B.C. of pump: static pressure
Inlet B.C. of pump: total pressure
Outlet B.C. of pump: static pressure

In a research conducted by Marigota et al. [17] it was depicted that if the second boundary condition is chosen for transient simulation of pumps, five impeller revolutions are required to obtain periodic unsteady solution convergence. Afterwards, Gonzalez et al. [19] reported that when the third boundary condition is opted, ten impeller revolutions are required for obtaining the same convergence. Eventually, Spence et al. [18] employed all of these options and observed that the most accurate and fastest convergence is obtained by using the second boundary condition. Therefore, the second boundary condition was adopted in this research.

At the solid surface of blade, hub, shroud, volute casing and inlet pipe, no-slip wall conditions were applied. The rotating (impeller) and stationary (the fluid inside the casing and the inlet pipe) zones are connected through the frozen rotor interface in steady-state and transient rotor-stator in transient solution. Since one-third of flow over the impeller is simulated, the rotational periodicity boundary condition is applied at the outer sides of the modeled domain. The settings were common in all three mentioned cases of simulation groups.

The mesh independency study of five mesh densities was performed by analyzing head and efficiency of the pump. Table 2 depicts that when mesh elements are increased from 3,349,340 to 4,395,012, the difference of head and efficiency is less than 0.5%. Ultimately, a grid with 3,349,340 elements was chosen.

It is obvious from the Fig. 2 that the distribution of y^+ at the volute and the blade surface is suitable using the selected turbulence model [20].

The vane tip fault that is one of the most prevalent faults in centrifugal pumps was implemented by cutting a small part of the blade tips of the impeller. Fig. 3 shows the impeller used in the simulation with this fault.

Two phases, water and water vapor were defined for implementing the cavitation defect in Ansys CFX software. A homogeneous multiphase model is selected and the evolution of cavity is described by using cavitation type mass transfer. In accordance with the test temperature, saturation pressure is selected as a constant. Total pressure at the entrance side with zero volume fraction of vapor was specified as inlet boundary condition. The outlet boundary condition, mass flow rate, was applied at the outlet of the volute. The initial calculation of steady cavitation flow is converged under a certain operating condition. After that, subsequent calculations are done by decreasing the inlet pressure of the pump, step by step. Then, the result is used as the initial flow field in unsteady flow simulation.

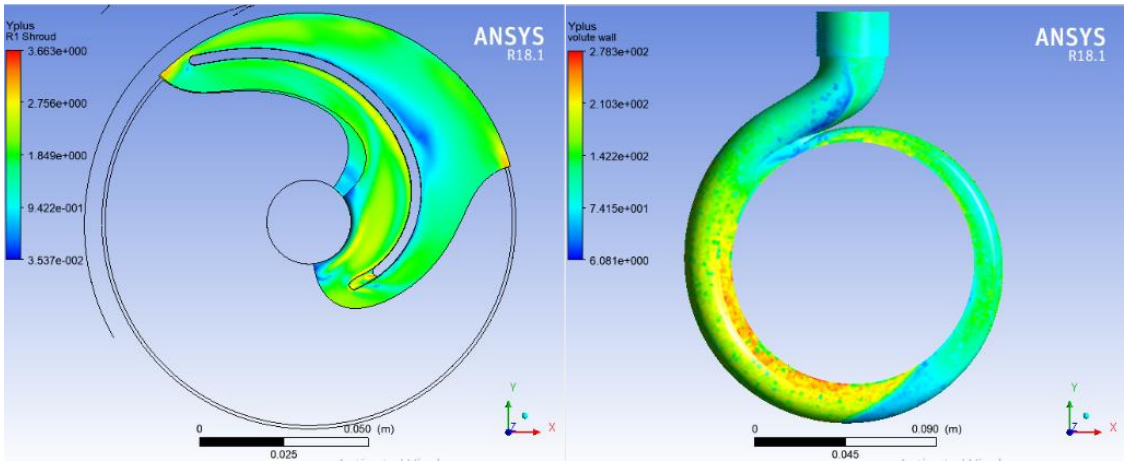

Fig. 2. Distribution of at the volute and the blade surface.

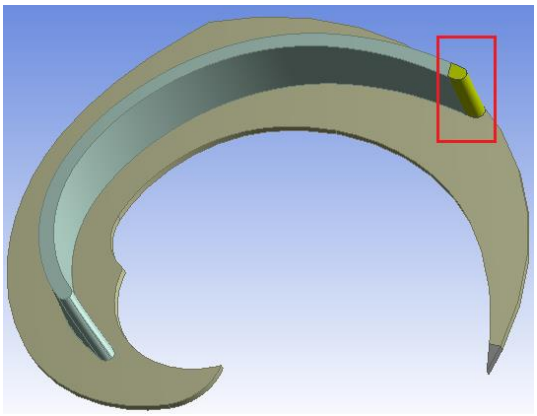

Fig. 3. Cutted blade.

3- LUMPED-PARAMETER MODEL OF INDUCTION MOTOR

The electrical motor that is in charge of driving the centrifugal pump studied in this research was a single-phase induction motor with a squirrel cage rotor and permanent capacitor. Table 3 presents the parameters of this motor. The phase shift and the starting torque that are required in the starting phase are provided by the capacitor. Furthermore, the capacitor improves the power factor, efficiency and torque pulsations during normal running. The stator is here modeled in two phases, main and auxiliary windings of the stator. Fig. 1 shows the schematic circuit for this motor.

As stated above, the rotor of this motor is of the squirrel cage type with bars placed in rotor slots and short-circuited at the two ends by a ring. We can model the rotor in two-phase style for ameliorating the modeling procedure. The relation between current and flux linkage is [21]:

$$\begin{bmatrix} \lambda_{main} \\ \lambda_{aux} \\ \lambda_1 \\ \lambda_2 \end{bmatrix} = \mathbf{K} \begin{bmatrix} \mathrm{i}_{main} \\ \mathrm{i}_{aux} \\ \mathrm{i}_1 \\ \mathrm{i}_2 \end{bmatrix} \tag{1}$$

where:

$$\mathbf{K} = \begin{bmatrix} L_{main} & 0 & L_{main,1}(\theta) & L_{main,2}(\theta) \\ 0 & L_{aux} & L_{aux,1}(\theta) & L_{aux,2}(\theta) \\ L_{main,1}(\theta) & L_{aux,1}(\theta) & L_r & 0 \\ L_{main,2}(\theta) & L_{aux,2}(\theta) & 0 & L_r \end{bmatrix}$$

Table 3. Induction Motor Parameters

Parameters	Unit	Value
Nominal Power	W	746
Frequency	Hz	50
Main winding stator resistance	Ohm	1.2
Main winding stator inductance	H	4.5e-4
Main winding rotor resistance	Ohm	1.82
Main winding rotor inductance	H	6.2e-4
Main winding mutual inductance	H	0.105
Auxiliary winding stator resistance	Ohm	9.14
Auxiliary winding stator inductance	H	25e-4
Pole pairs	-	1
Permanent capacitor	F	25e-6

λ_{main} main-winding ux linkage (Weber);
λ_{aux} auxiliary-winding ux linkage (Weber);
λ_1 rotor phase-1 winding ux linkage (Weber);
λ_2 rotor phase-2 winding ux linkage (Weber);
i_{main} main-winding current (A);
i_{aux} auxiliary-winding current (A);
i_1 rotor phase-1 winding current (A);
i_2 rotor phase-2 winding current (A);
L_{main} self-inductance of the main winding (H);
L_{aux} self-inductance of the auxiliary winding (H);
L_r self-inductance of the equivalent rotor winding (H);
$L_{main,1}(\theta)$ mutual inductance between the main winding and equivalent rotor winding 1 (H);
$L_{main,2}(\theta)$ mutual inductance between the main winding and equivalent rotor winding 2 (H);
$L_{aux,1}(\theta)$ mutual inductance between the auxiliary winding and equivalent rotor winding 1 (H);
$L_{aux,2}(\theta)$ mutual inductance between the auxiliary winding and equivalent rotor winding 2 (H);
θ rotor electrical angle (radians);

By inspecting the equivalent circuit of the motor provided in [21], voltage can be found as:

$$v_{main} = i_{main}R_{main} + \frac{d\lambda_{main}}{dt} \quad (2)$$

$$v_{aux} = i_{aux}R_{aux} + \frac{d\lambda_{aux}}{dt} \quad (3)$$

$$v_1 = 0 = i_1 R_r + \frac{d\lambda_{r1}}{dt} \quad (4)$$

$$v_2 = 0 = i_2 R_r + \frac{d\lambda_{r2}}{dt} \quad (5)$$

in which v_{main}, v_{aux}, v_1 and v_2 are main, auxiliary, rotor phase-1 and rotor phase-2 winding voltage and R_{main}, R_{aux}, R_r and the resistance of main, auxiliary, and rotor winding respectively. As mentioned, rotor windings are short-circuited and thus, their voltages are set to be equal to zero.

The electrical torque generated by the motor can be found by taking derivative of the co-energy relation regarding the rotor angle, which yields [21]:

$$\begin{aligned} T_e &= i_{main}i_{r1}\frac{dL_{main,r1}(\theta_{me})}{d\theta_{me}} + i_{main}i_{r2}\frac{dL_{main,r2}(\theta_{me})}{d\theta_{me}} + \\ &i_{aux}i_{r1}\frac{dL_{aux,r1}(\theta_{me})}{d\theta_{me}} + i_{aux}i_{r2}\frac{dL_{aux,r2}(\theta_{me})}{d\theta_{me}} \\ &= \left(\frac{poles}{2}\right)[L_{main,r}\left(i_{main}i_{r1}\sin(\theta_{me}) + i_{main}i_{r2}\cos(\theta_{me})\right) + \\ &L_{aux,r}\left(i_{aux}i_{r1}\cos(\theta_{me}) - i_{aux}i_{r2}\sin(\theta_{me})\right)] \end{aligned} \quad (6)$$

Current and voltage of the stator in the steady-state working conditions are:

$$v_{main} = \sqrt{2}V_{main}\cos(\omega_e t + \varphi_{main}) = \mathrm{Re}\left[\sqrt{2}\hat{v}_{main}e^{i\omega_e t}\right] \quad (7)$$

$$v_{aux} = \sqrt{2}V_{aux}\cos(\omega_e t + \varphi_{aux}) = \mathrm{Re}\left[\sqrt{2}\hat{v}_{aux}e^{i\omega_e t}\right] \quad (8)$$

$$i_{main} = \sqrt{2}I_{main}\cos(\omega_e t + \phi_{main}) = \mathrm{Re}\left[\sqrt{2}\hat{I}_{main}e^{i\omega_e t}\right] \quad (9)$$

$$i_{aux} = \sqrt{2}I_{aux}\cos(\omega_e t + \phi_{main}) = \mathrm{Re}\left[\sqrt{2}\hat{I}_{aux}e^{i\omega_e t}\right] \quad (10)$$

Where:

v rms voltage amplitude (V);

i rms current amplitude (A);

φ, ϕ phase angle;

$\hat{V}$ complex rms voltage amplitude (V);

$\hat{I}$ complex rms current amplitude (A);

The relation between current and flux linkage for the main and auxiliary windings of the stator in the phasor form could be found by eliminating the rotor current from Eqs. (4), (5), (8), and (9) [22]. The resultant equation is:

$$\lambda_{main} = \mathrm{Re}\left[\hat{\lambda}_{main} e^{i\omega t}\right] \tag{11}$$

$$\lambda_{aux} = \mathrm{Re}\left[\hat{\lambda}_{aux} e^{i\omega t}\right] \tag{12}$$

$$\hat{\lambda}_{main} = \left[L_{main} - jL^2_{main,r}(\hat{K}^+ + \hat{K}^-)\right]\hat{I}_{main} + L_{main,r}L_{aux,r}(\hat{K}^+ - \hat{K}^-)\hat{I}_{aux} \tag{13}$$

$$\hat{\lambda}_{aux} = -L_{main,r}L_{aux,r}(\hat{K}^+ - \hat{K}^-)\hat{I}_{main} + \left[L_{aux} - jL^2_{aux,r}(\hat{K}^+ + \hat{K}^-)\right]\hat{I}_{aux} \tag{14}$$

$$\hat{K}^+ = \frac{s\omega_e}{2(R_r + js\omega_e L_r)} \tag{15}$$

$$\hat{K}^- = \frac{(2-s)\omega_e}{2(R_r + j(2-s)\omega_e L_r)} \tag{16}$$

and, s , the rotor slip is defined as:

$$s = \frac{(\omega_e - \omega_m)}{\omega_e} \tag{17}$$

in which ω_e denotes the electrical frequency and ω_m is the mechanical speed of the rotor.

In a permanent capacitor motor, shown in Fig. 1, auxiliary winding voltage, capacitor voltage, and supply voltage are related as:

$$V_c + V_{aux} = V \tag{18}$$

where, V_c , the capacitor voltage could be obtained from:

$$V_c = -jI_{aux}X_c \tag{19}$$

in which:

$$X_c = -\frac{1}{\omega_e C} \tag{20}$$

Here, by combining Eqs. (13) and (14) with (7) and (8), $\hat{I}_{main}$ and $\hat{I}_{aux}$ could be calculated as:

$$\begin{bmatrix} R_{aux} + jX_c + j\omega_e\left[L_{aux} - jL^2_{aux,r}(\hat{K}^+ + \hat{K}^-)\right] & -j\omega_e\left[L_{main}jL_{aux,r}(\hat{K}^+ - \hat{K}^-)\right] \\ j\omega_e\left[L_{main}jL_{aux,r}(\hat{K}^+ - \hat{K}^-)\right] & R_{aux} + jX_c + j\omega_e\left[L_{aux} - jL^2_{aux,r}(\hat{K}^+ + \hat{K}^-)\right] \end{bmatrix}\begin{bmatrix} \hat{I}_{main} \\ \hat{I}_{aux} \end{bmatrix} = \begin{bmatrix} V_c \\ -V_c \end{bmatrix} \tag{21}$$

Eventually, the stator windings current can be obtained by inversing the matrix coefficients in Eq. (21), and using that, the total current passing the electrical terminal could be found.

Eq. (21) provides an intuition about the connection between mechanical and electrical terminals. It could be easily deducted that a change in the mechanical shaft speed will have an influence on the terminal current through change in slip. Besides, the relationship between rate of change of speed and all torques applied on the rotating shaft could be obtained using Newton's 2nd law as:

$$J_m \frac{d\omega_m}{dt} = T_e - T_l \tag{22}$$

T_e produced torque by induction motor (N.m);

T_l load torque of pump (N.m);

J_m sum of Impeller, rotor, and shaft inertia (kg.m^2);

Therefore, the mechanical faults such as impeller defects, cavitation, etc. will have an effect on the load torque, and through that, will influence the electrical terminal by changing the current signal.

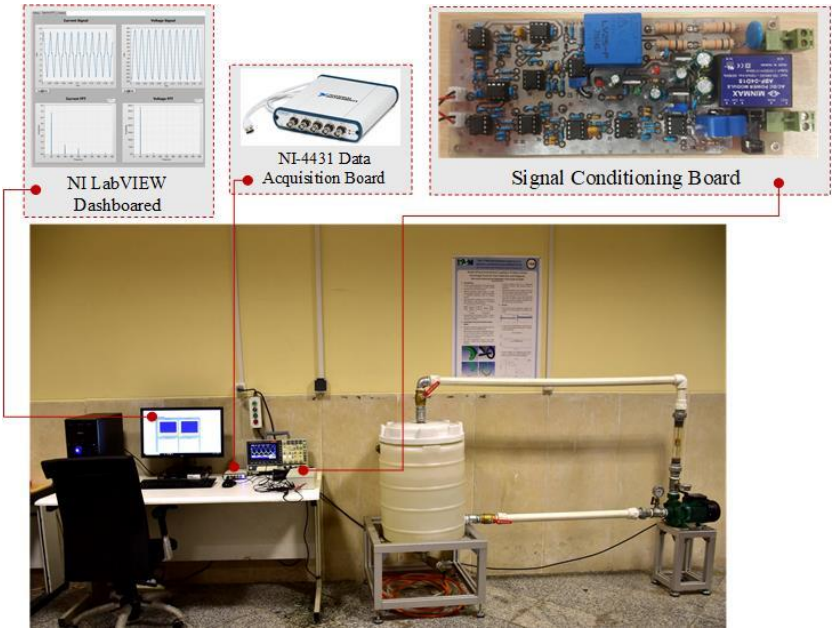

Fig. 4. Impeller with vane tip fault

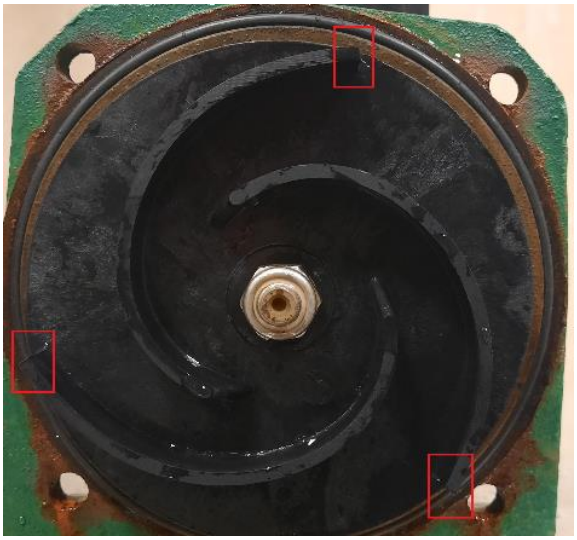

Fig. 5. Impeller with vane tip fault.

4- EXPERIMENTAL INVESTIGATION

In order to validate the obtained numerical results, output head and flow rate should be measured. Also, for portraying the impact of introduced faults on the pump operation, data should be acquired from current signal of the motor in healthy condition as well as after introducing cavitation and defected impeller faults. For this end, a hydraulic closed rig was designed and implemented for performing the experimental tests. Fig. 4 shows the hydraulic circuit. The pump used in this setup is similar to the simulated pump and is driven by a squirrel cage induction motor with the constant speed of 2900 rpm. Flow rate is measured using a rotameter installed on the pump outlet. Pressure values before and after the pump are measured using pressure gauges installed in the inlet and outlet of the pump. In this research, data acquisition is performed utilizing a NI-4431 board that is equipped with 5 channels. Current signal is measured using a current sensor and is passed through an 8th order Chebbyshev anti-aliasing filter which is shown in Fig. 4. Sampling rate is chosen to be 8 kHz.

The vane tip fault is introduced by cutting all blades of the impeller equally and similar to the simulation. Fig. 5 shows the impeller after introducing this fault.

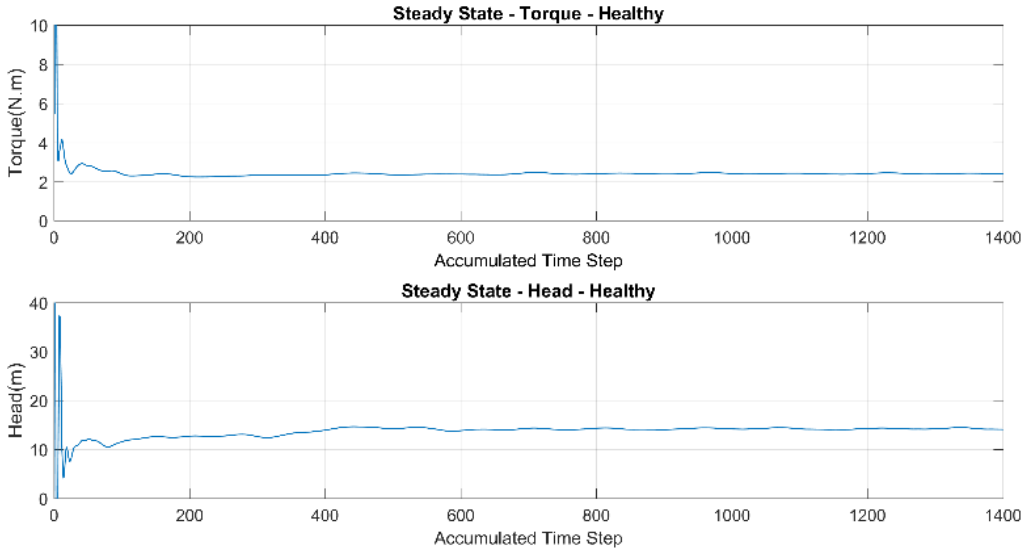

Fig. 6. Convergence of the head and torque to a constant value.

Table 4. Validation of Simulation Results at BEP with Following Condition: $Q_{BEF} = 12m^3/h$ and $\omega = 2900$ rpm

	Eefficiency	Head (m)
Pump catalog value	66 %	14.50
Predicted value	62.4 %	14.25
Error	5.4 %	1.7 %

In order to induce cavitation in the system, the valve in the inlet of the pump was closed gradually, while flow rate was increased simultaneously using the upstream valve. The instant the flow cannot increase any further and a sudden drop in the pump head is observed, cavitation has occurred, which causes severe noise and vibration in the system.

5- RESULTS

A.Ansys CFX Model Validation

The head and torque obtained from the steady-state simulation converge to constant values which are shown in Fig. 6. The head predicted from the simulation at BEP at 2900 is compared with the head reported in pump catalog in Table 4. From the table, it can be observed that the maximum relative error of the prediction is about 5%. Hence, we can conclude that the catalog data and the numerical results are in suitable agreement.

Fig. 7 shows the curves of the pump head according to the available net positive suction head $NPSH_a$ that obtained from experiment test and simulation in cavitation condition $NPSH_a$ which is shown in the horizontal axis is defined as:

$$NPSH_a = \frac{(P_{inlet} - P_v)}{\rho g} \quad (23)$$

where P_{inlet} is the pump inlet pressure and P_v is the vapor pressure. The result of numerical simulation corresponds well with the experimental data especially in the rapid downward trend of $NPSH_a$ decline. As can be seen in the Fig. 7, the head of the pump remains constant with the reduction of $NPSH_a$ until it reaches to a specific value called the required net positive suction head ($NPSH_r$). In this step, the mean head of pump reduced by three percent (3%), the first vapor bubbles appear in the flow. From the Fig. 7 it can be seen that the experimental $NPSH_r$ is 5 m, while it is estimated one was 5.3 m resulting in a deviation of about 6%.

B.Effect of Vane Tip Fault on the Pump Performance

1)Study of time domain results

Fig.8 and Fig.9 compare the load torque of the blades and the head of the pump in healthy and faulty transient simulations. Inspecting the figure, it can be deducted that the vane tip fault alters the average of the load torque and the head of the pump substantially.

It is known that rotation of the pump impeller increases the fluid speed. When the fluid moves from the casing toward the outlet pipe, the fluid speed drops and its pressure increases. Since cutting a part of the blade results in less increase of the fluid speed, the pressure increase in the pump outlet will also diminish. Therefore, after introducing the blade vane tip

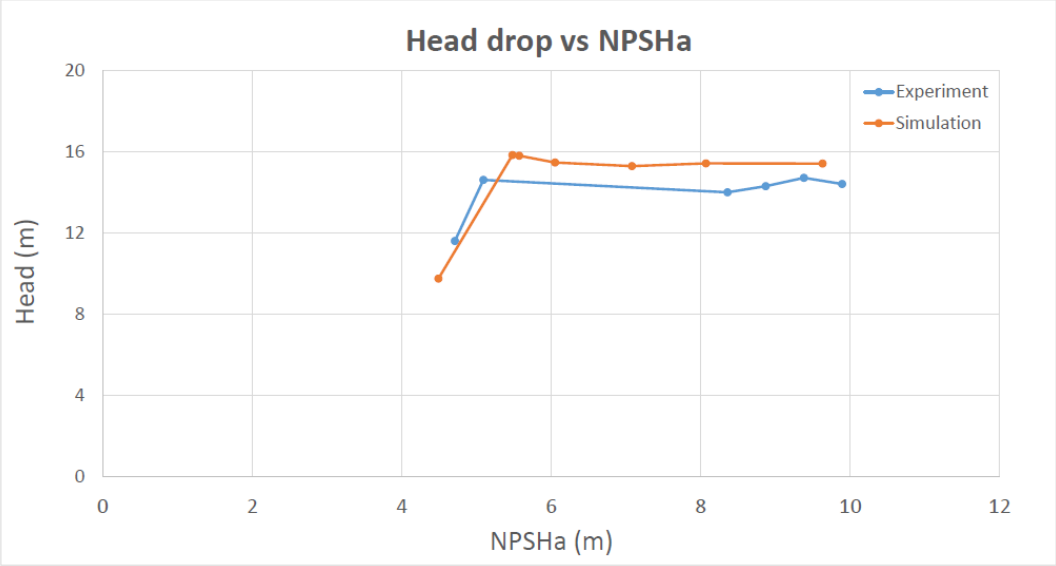

Fig. 7. Comparison of measured and predicted for cavitation test.

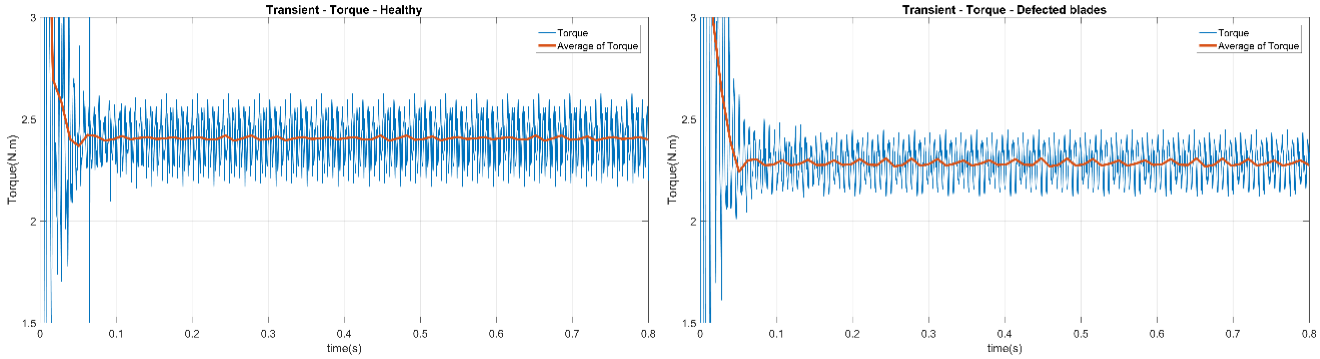

Fig. 8. Comparison of load torque in healthy (left) and defected blades (right) simulations.

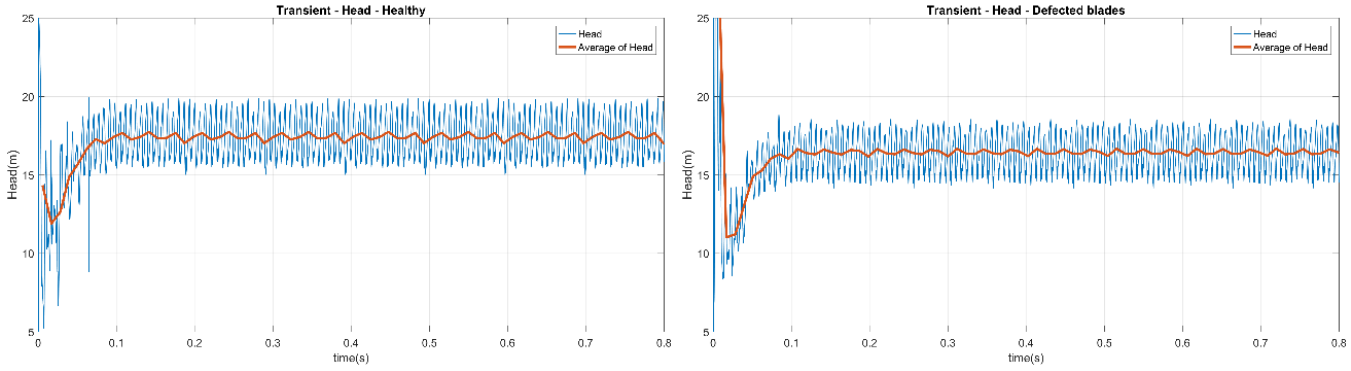

Fig. 9. Comparison of head in healthy (left) and defected blades (right) simulations.

Table 5. Averaged head and load torque in healthy and defected blades simulations

	Head (m)	Load Torque (N.m)
Healthy	17.428	2.406
Defected blades	16.45	2.281
diff %	5.61 %	5.20 %

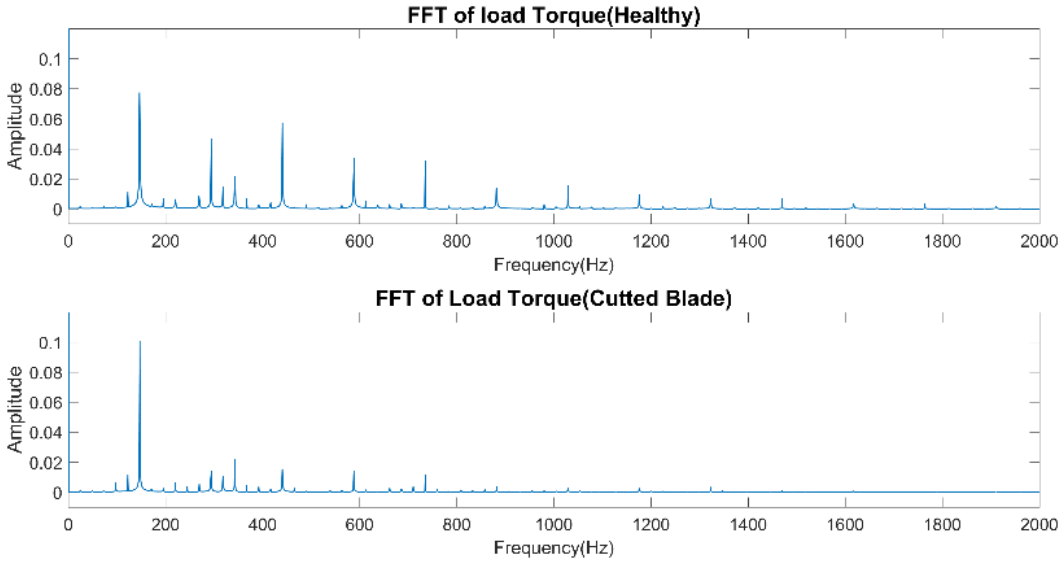

Fig. 10. FFT of load torque signal of simulation in healthy (top) and defected blades (bottom) condition.

fault, the output head of the pump is expected to shrink. Table 5 shows the change in the average of the head and load torque on the blades after the blade tip is cut with regard the healthy condition.

2)Study of frequency domain results

In order to inspect changes in the frequency domain of the load torque signal, its Fast Fourier Transform (FFT) was calculated for the two simulations. The results of applying this transform are provided in Fig. 10. It can be seen that the first main frequency component is at *BPF* (147Hz) which is 3 times the fundamental frequency *fs* (49Hz). This is in compliance with our expectation since there are three blades in the impeller. It can be observed that in the faulty condition, the first frequency component has increased, while components at higher harmonics have reduced.

C.Effect of Cavitation on the Pump Performance

1)Study of time domain results

Cavitation in the centrifugal pumps is often diagnosed by its harmful influences such as severe decline in the hydraulic performance and generated noise and vibrations. In Figs. 11 and 12, the load torque on the blades and the output head of the pump that are obtained from the results of the simulation in the transient condition in healthy status and with the presence of cavitation. As it can be observed from Fig. 12, after introducing cavitation, the head of the pump has severely slackened. Furthermore, Fig. 11 depicts a decrease in the average load torque on the blades, as well as its severe fluctuations that are caused by the noise resulted from cavitation.

2)Study of frequency domain results

Fig. 13 shows the FFT obtained from the load torque on the blades in the healthy condition and under the presence of cavitation. It can be observed that the torque amplitude has increased compared to the healthy status that is produced by intense noise and vibrations created by cavitation.

Effect of Vane Tip Fault on the Motor Current

Vane tip fault will lead to a decrease in the pump head and thus, power and current of the motor. As it can be observed from Fig. 14, the amplitude of the motor current in the fundamental frequency (*fs* = 49Hz) and in blade passing frequency (*BPF* = 147Hz) has decreased compared to the healthy condition. A better depicture of the effect that the defective impeller has on the frequency domain, the difference between a healthy and faulty spectrum is provided in Fig. 15.

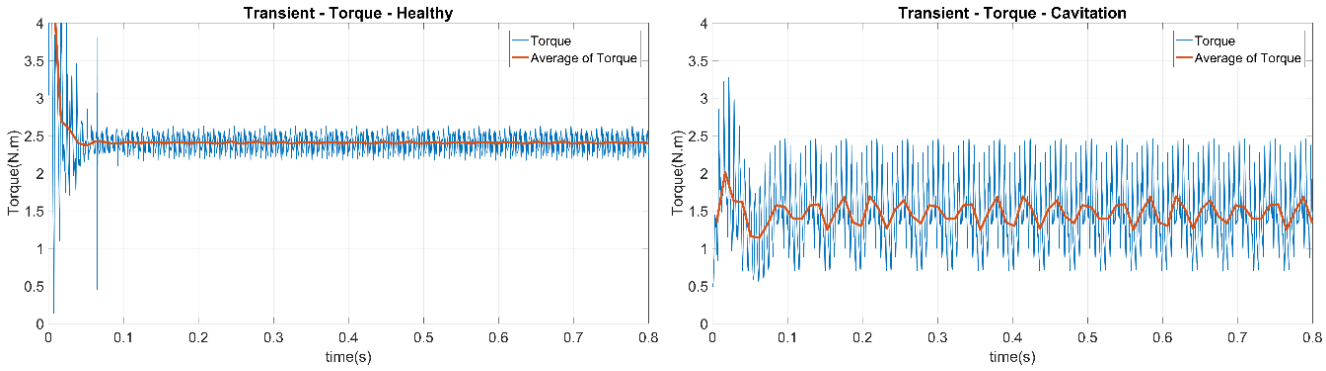

Fig. 11. Comparison of load torque in healthy (left) and cavitation (right) simulations.

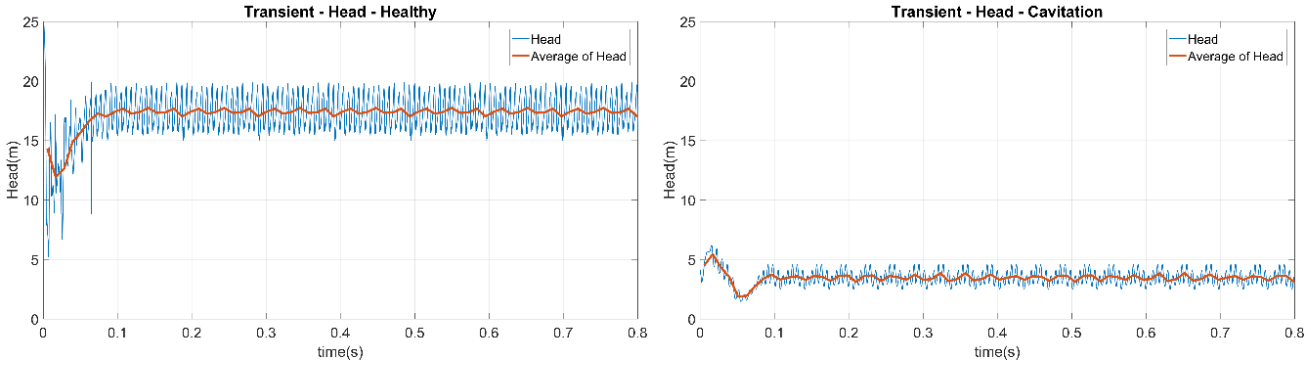

Fig. 12. Comparison of head in healthy (left) and cavitation (right) simulations.

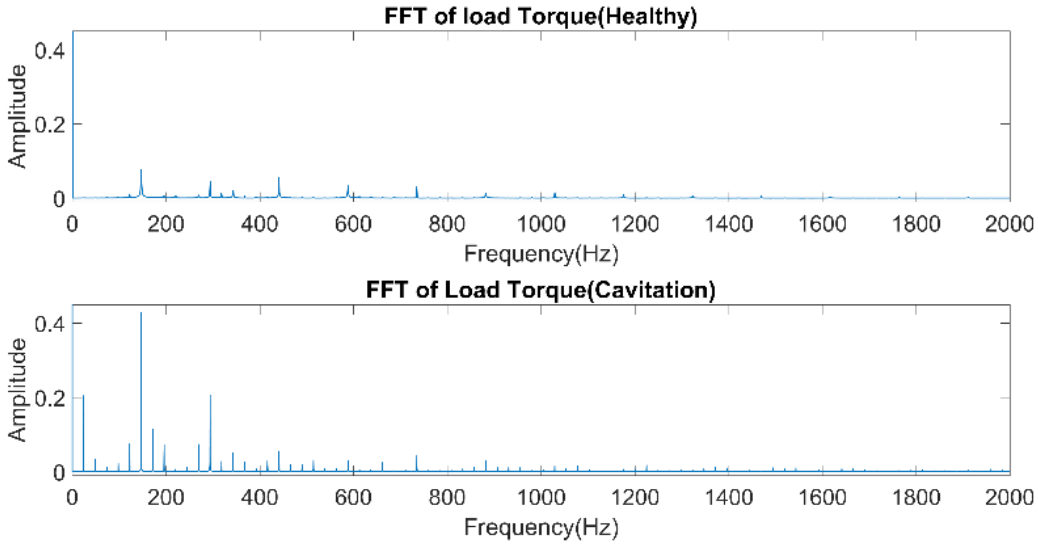

Fig. 13. FFT of load torque signal of simulation in healthy (top) and cavitation (bottom) condition.

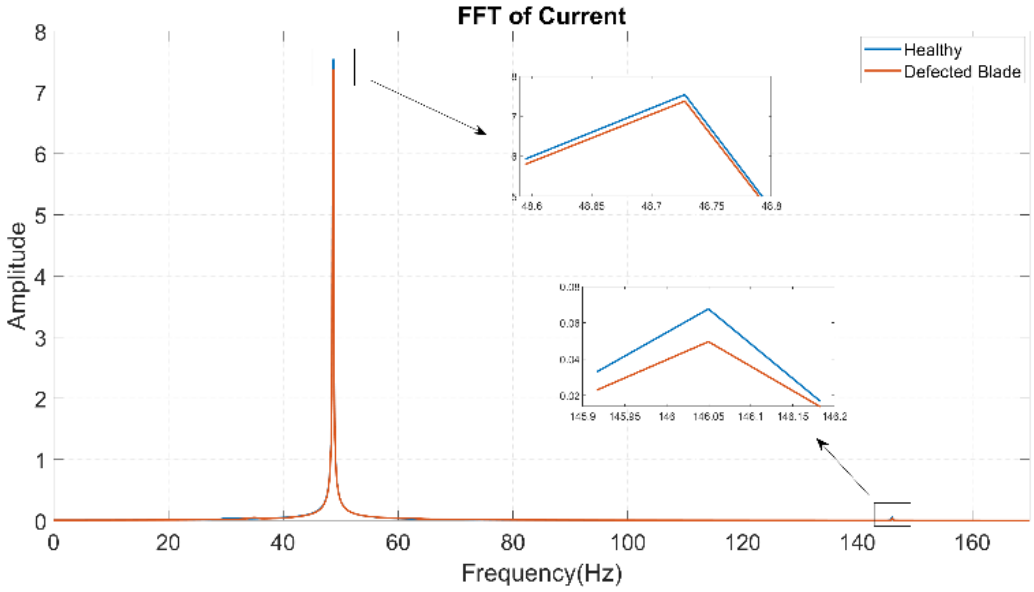

Fig. 14. Current FFT in healthy and defected blades condition (simulation).

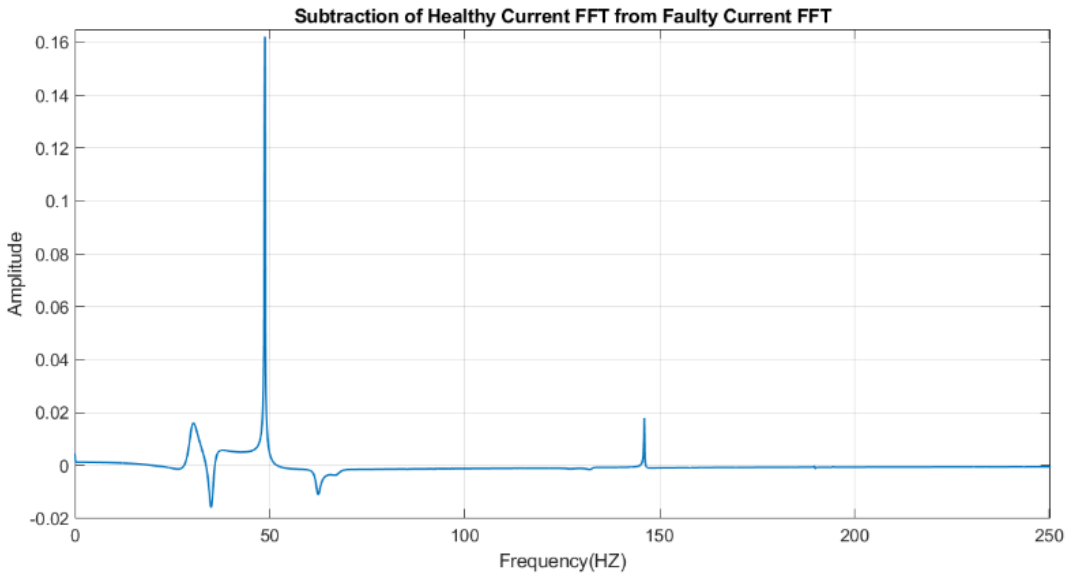

Fig. 15. Subtraction of healthy current FFT from faulty current FFT.

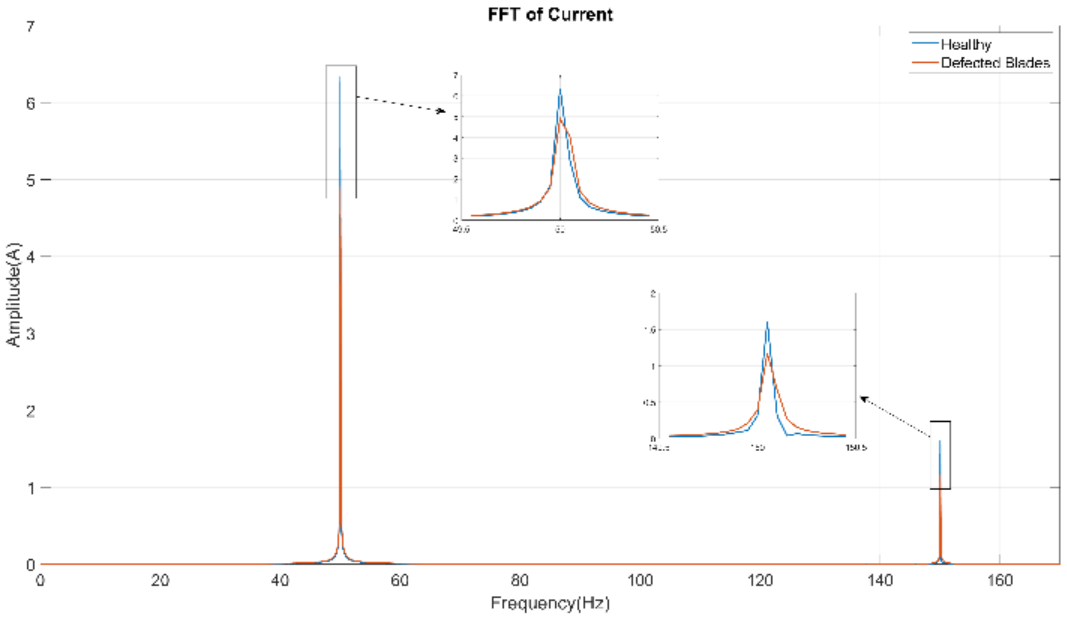

Fig. 16. Current FFT in healthy and defected blades condition (experiment).

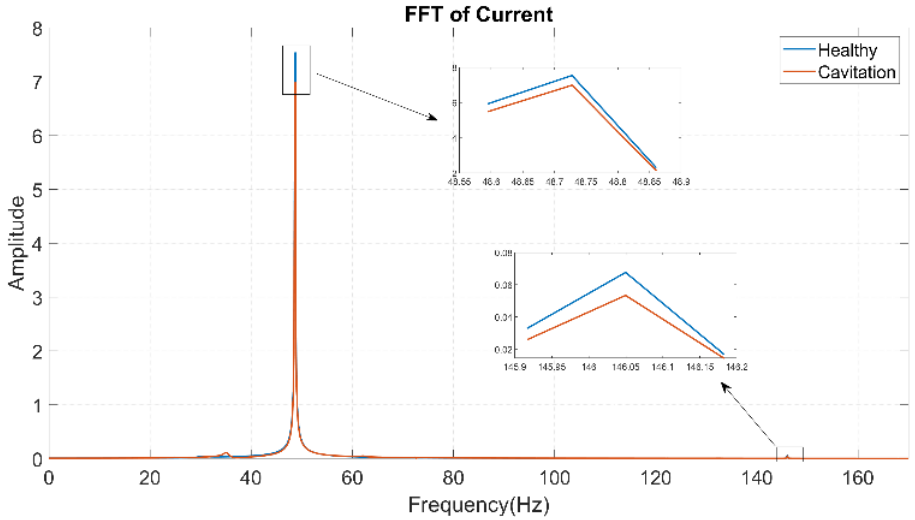

Fig. 17. Current FFT in healthy and cavitation condition (simulation).

The correctness of this issue is certified by the experimental test performed at the same flow rate (Fig.16). In Fig. 16, the amplitude of the current in 49 Hz and 147 Hz frequencies are also compared for the experimental results in the healthy condition and the presence of vane tip fault. The shrink in the current amplitude in these two frequencies ascertains the correctness of the modeling.

D.Effect of Cavitation on the Motor Current

Cavitation causes a decrease in the output head of the pump and thus, reduces the power and current of the motor. As can be seen, the current measured from the experimental test is also decreased in the presence of cavitation. In Figs. 17 and 18, reduction in the amplitude of current at the frequency of *fs* and *BPF* in the presence of cavitation compared to the healthy status are shown. These results also demonstrate the validity of the developed model.

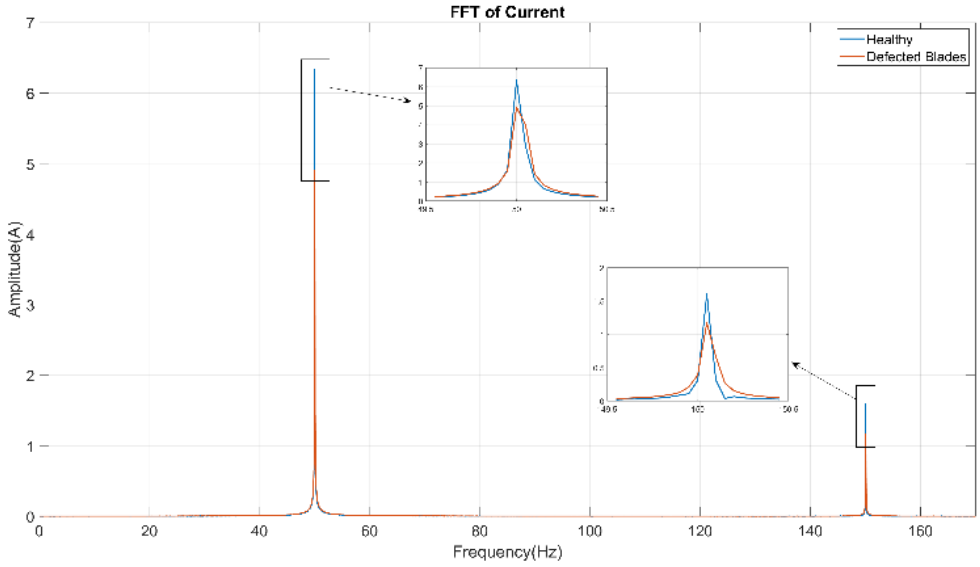

Fig. 18. Current FFT in healthy and cavitation condition (experiment).

6- CONCLUSION

In this paper, a comprehensive model of the electromechanical coupling in a motor-driven centrifugal pump was developed to demonstrate the impact of common pump faults, including vane tip fault and cavitation, on motor electrical signals. The lumped-parameter approach was employed to model the induction motor and computational fluid dynamic techniques were used to simulate the fluid-solid interaction in the pump. The results of CFD analysis showed that the defective blades and cavitation phenomenon reduce the load torque average on the blades and the output head of the pump. These defects eventually distort the shaft speed harmonics, which in turn alter the motor current signal obtained from the lumped-parameter model of the motor. Also, the frequency spectrum of the load torque and motor current signals obtained under the healthy and faulty conditions were compared. The results showed the reduction of the amplitude of current at fundamental frequency (fs = 49Hz) and blade passing frequency (BPF = 147Hz) in the presence of cavitation and vane tip faults compared to the healthy status. A closed hydraulic test rig was built to collect voltage and current signals in different operating conditions. An experimental test rig was developed for the implementation of different operating condition of the pump where voltage and current signals were collected at each stage. A good agreement obtained between the experimental and numerical results under the healthy and faulty conditions. From the analysis of the current signals collected from healthy and defective blades in frequency domain, it was observed that the amplitude of the motor current in the fundamental and blade passing frequency has decreased compared to the healthy condition. Similar result was also obtained for cavitation condition. In addition, the comparison of these results with the FFT of current obtained from the simulation demonstrate the validity of the developed model. The agreement between the model and empirical results show that we can reliably use the proposed multi-domain modeling platform for obtaining insight into motor-driven centrifugal pumps and developing condition monitoring algorithms in situations where the experimental data are not readily available.

References

[1] G. Mousmoulis, N. Karlsen-Davies, G. Aggidis, I. Anagnostopoulos, D. Papantonis, Experimental analysis of cavitation in a centrifugal pump using acoustic emission, vibration measurements and flow visualization, European Journal of Mechanics-B/Fluids, 75 (2019) 300-311.

[2] A.R. Al-Obaidi, Investigation of effect of pump rotational speed on performance and detection of cavitation within a centrifugal pump using vibration analysis, Heliyon, 5(6) (2019) e01910.

[3] A. Choudhary, D. Goyal, S.L. Shimi, A. Akula, Condition monitoring and fault diagnosis of induction motors: A review, Archives of Computational Methods in Engineering, 26 (2019) 1221-1238.

[4] R. Greene, D. Casada, C. Ayers, Detection of pump degradation, Nuclear Regulatory Commission, 1995.

[5] R. Kryter, H. Haynes, Condition monitoring of machinery using motor current signature analysis, Oak Ridge National Lab., 1989.

[6] C.S. Kallesoe, V. Cocquempot, R. Izadi-Zamanabadi, Model based fault detection in a centrifugal pump application, IEEE transactions on control systems technology, 14(2) (2006) 204-215.

[7] T. Dalton, R. Patton, Model-based fault diagnosis of a two-pump system, Transactions of the Institute of Measurement and Control, 20(3) (1998) 115-124.

[8] K. Kim, A.G. Parlos, R.M. Bharadwaj, Sensorless fault diagnosis of induction motors, IEEE Transactions on Industrial Electronics, 50(5) (2003) 1038-1051.

[9] C. Kallesøe, Fault detection and isolation in centrifugal pumps, Department of Control Engineering, Aalborg University, 2005.

[10] M.L. Nilugal, K.V. Karanth, N. Madhwesh, A critical review on the application of computational fluid dynamics in centrifugal turbomachines, in: Journal of Physics: Conference Series, IOP Publishing, 2020, pp. 012012.

[11] S. Shah, S. Jain, R. Patel, V. Lakhera, CFD for centrifugal pumps: a review of the state-of-the-art, Procedia Engineering, 51 (2013) 715-720.

[12] E. Bacharoudis, A. Filios, M. Mentzos, D. Margaris, Parametric study of a centrifugal pump impeller by varying the outlet blade angle, The Open Mechanical Engineering Journal, 2(1) (2008).

[13] S. Shah, S. Jain, V. Lakhera, CFD based flow analysis of centrifugal pump, Proceedings ofInternational Conferenceon Fluid Mechanics and Fluid Power. Chennai, India, paper# TM08, (2010).

[14] A. Zabihi, Fault Detection of Centrifugal Pump: a Comparison of Fluid Pressure Fluctuation Sim- ulation with Mesuearment of Casing Vibration, University of Tehran, 2017.

[15] J. Lu, S. Yuan, Y. Luo, J. Yuan, B. Zhou, H. Sun, Numerical and experimental investigation on the development of cavitation in a centrifugal pump, Proceedings of the Institution of Mechanical Engineers, Part E: Journal of Process Mechanical Engineering, 230(3) (2016) 171-182.

[16] T. Lei, Z.B. Shan, C.S. Liang, W.Y. Chuan, W.B. Bin, Numerical simulation of unsteady cavitation flow in a centrifugal pump at off-design conditions, Proceedings of the Institution of Mechanical Engineers, Part C: Journal of mechanical engineering science, 228(11) (2014) 1994-2006.

[17] E. Blanco-Marigorta, J. Fernández-Francos, J.L. Parrondo-Gayo, C. Santolaria-Morros, Numerical simulation of centrifugal pumps, in: Proc. ASME Fluids Engineering Summer Conference (FEDSM'00), 2000.

[18] R. Spence, J. Amaral-Teixeira, Investigation into pressure pulsations in a centrifugal pump using numerical methods supported by industrial tests, Computers & fluids, 37(6) (2008) 690-704.

[19] J. Gonza´ lez, C. Santolaria, F. Castro, M.T. Parra, Numerical model for the unsteady flow behaviour inside a double suction pump, in: Fluids Engineering Division Summer Meeting, 2003, pp. 1149-1155.

[20] C. ANSYS, ANSYS CFX Solver Modeling Guide, Release 15.0, Volume, 455 (2013) 162-168.

[21] A.E. Fitzgerald, C. Kingsley, S.D. Umans, Electric machinery, (2003).

[22] S.D. Umans, Steady-state, lumped-parameter model for capacitor-run, single-phase induction motors, IEEE Transactions on Industry Applications, 32(1) (1996) 169-179.

HOW TO CITE THIS ARTICLE

Z. Araste, M. Jamimoghaddm, A. Sadighi, Multi-Domain Modeling Platform for Electrical-Signature-Based Condition Monitoring of Motor-Driven Pumps, AUT J. Mech Eng., 7(1) (2023) 73-88.

DOI: 10.22060/ajme.2023.21285.6033